

# Radiative Transfer in Luminescent Solar Concentrators

Sha Li, Sophia Haussener\*

*Laboratory of Renewable Energy Science and Engineering, EPFL, Station 9, Lausanne 1015, Switzerland*

## Highlights

- A self-consistent modelling framework of radiative transfer in LSC is presented.
- Application to Lumogen F Red 305 dye doped in PMMA is demonstrated.
- Transmission loss is the dominant loss mechanism and accounts for 76–92%.
- 12.5% external photon efficiency is predicted at dye concentration of 0.0002 mol/L.

## Abstract

A luminescent solar concentrator (LSC) offers a viable solution to spectrally convert and concentrate both direct and diffuse sunlight without the need for tracking. Its potential for commercialization is currently limited by the optical performance. A detailed understanding of the effects of both waveguide and luminophore properties is crucial for designing efficient LSCs. Herein, a self-consistent modelling framework of radiative transfer in LSCs is presented to analyze these effects by incorporating all properties at multiple length scales. A modified radiative transfer equation (RTE) is derived capturing the requirement that both photon absorption and photoluminescence quantum yield (PLQY) should occur simultaneously to trigger the PL emission. The Monte Carlo method is used to solve this modified RTE along with its boundary conditions. This framework is further employed to investigate the performance of LSCs doped with Lumogen F Red 305 dye. For the realistic scenarios, the transmission loss forms the main loss mechanism and accounts for 76.2–92.1% depending on the specific dimensions and LFR305 doping. An external photon efficiency of 12.5% is predicted for an LSC of  $10 \times 10 \times 0.5$  cm<sup>3</sup> with a dye concentration of  $2 \times 10^{-4}$  mol/L. As to the hypothetical scenarios, the waveguide refractive index affects both the top reflection and the escape cone losses, while by contrast, the PLQY and the Stokes shift mainly affect the QY loss. Future efforts on LSC optimization should be directed towards reducing the transmission loss.

**Keywords:** luminescent solar concentrator, modified radiative transfer equation, Monte Carlo ray tracing, Lumogen F Red 305 dye, performance optimization

---

\* Corresponding author.

E-mail address: [sophia.haussener@epfl.ch](mailto:sophia.haussener@epfl.ch) (S. Haussener).

## 1. Introduction

A luminescent solar concentrator (LSC) is a promising photonic technology with potential applications in, for example, building-integrated photovoltaic structures, horticulture, photochemical reactors, or smart windows [1]. An LSC is typically composed of a waveguide doped or coated with well-quantified concentrations of one or more luminophore species, including organic dyes, inorganic phosphors, and quantum dots. Such a design allows the sunlight incident on the top surface to be absorbed by the luminophore(s), and then emitted at a different wavelength in the form of photoluminescence (PL), which will be transported to the edges via total internal reflection (TIR), thus achieving spectral conversion and light concentration (see **Fig. 1**). Compared with the conventional solar concentrating technologies, LSC offers the advantages of being able to utilize both direct and diffuse sunlight without tracking, and the flexibility to tune its PL emission spectrum by using different luminophores [1]. However, the LSC is not yet commercialized primarily due to its modest performance (record external photon efficiency so far is 11.7% [2]).

Computational models have been developed to predict the performance of a variety of LSC concepts. They fall into two categories: (i) thermodynamic modelling [3-6], and (ii) Monte Carlo (MC) ray tracing simulations [7-9]. The thermodynamic approach [3, 4] is essentially a 3D flux model claimed to not require the PL emission spectrum as an input, and its application is limited to those LSCs containing a single luminophore species [10]. However, this 3D flux model [3, 4] is obtained by performing integration over a range of solid angles for the radiative transfer equation (RTE) following the Schwarzschild–Milne Method, which is valid only for 1D, plane-parallel, and isotropic scattering media [11]. In addition, the RTE and the total radiative energy balance equation in Refs. [3, 5, 6] remain inconsistent, for the former cannot directly lead to the latter without providing the quantum yield (QY). It is thus desirable to develop a self-consistent, 3D modelling framework with respect to the spectral intensity as it travels within the LSC. As to the MC method, a number of ray tracing codes have been developed for specific LSCs with different geometries (planar, cylindrical, wedge-shaped, etc.), configurations (doped, thin-film, single layer, multi-layer, etc.), and luminophore properties (scattering, non-scattering) [7-9]. Nonetheless, most of the MC work is focused on detailing the history of each photon during the ray tracing process, and very few efforts have been made to describe the governing equation and boundary conditions in order to offer a clear picture of this problem. The lack of a well-stated governing equation in the MC method perhaps helps explain the fact that the thermodynamic model and the MC method have long been viewed as two different approaches [8, 10]. On the other hand, Kennedy et al. [10] showed that the predicted LSC performance based on these two methods is in agreement, which motivates us to hypothesize that the thermodynamic model and the MC method are equivalent. This is for example the case in the high-temperature thermal community where the MC method is widely employed to solve the conventional RTE for participating media in the absence of PL emission [11-13].

Herein, we first present a generic modelling framework of radiative transfer in LSCs by making an energy balance for the spectral intensity, with an emphasis on analyzing the PL emission from the luminophore. A modified RTE is derived, based on which the total radiative energy balance equation is obtained via integration over all solid angles and the full spectrum, thus demonstrating model self-consistency without additional input. To solve this modified RTE along with its associated boundary

conditions, the MC method is employed, which confirms the hypothesis that the thermodynamic model and the MC approach are equivalent. To demonstrate its application, this methodology was applied to a specific LSC composed of poly(methyl methacrylate) (PMMA) as the waveguide doped with a commercial dye Lumogen F Red 305 (LFR305). Its performance under both realistic and hypothetical scenarios are explored in order to offer insights on performance optimization.

## 2. Methodology

The model system is a 3D planar LSC doped with well-defined concentration of luminophores (e.g. with dyes, quantum dots, or phosphors) as shown in **Fig. 1**, which also illustrates the key light–matter interactions at multiple length scales. To model the radiative transport within the LSC, unlike the conventional RTE derived for a participating medium in the absence of PL emission, a modified RTE will be developed to account for this effect based on the radiative energy balance.

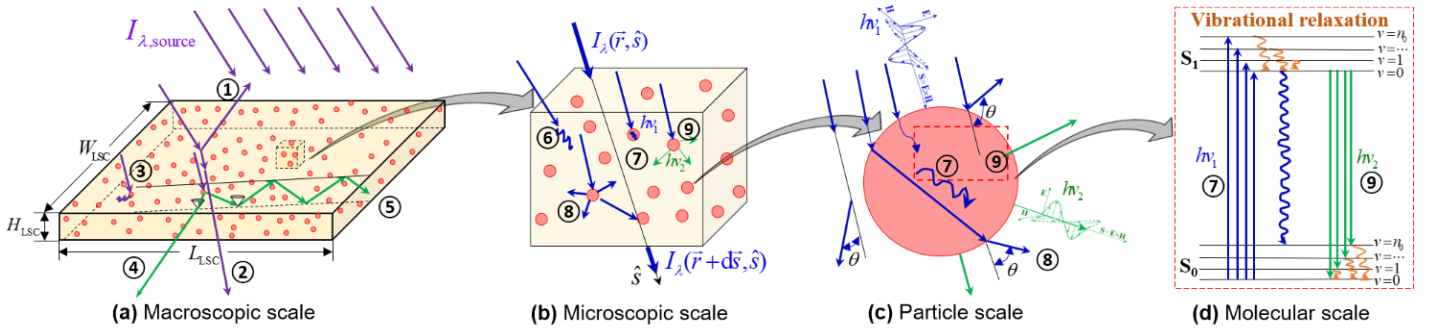


**Fig. 1.** Schematic of (a) the LSC model system irradiated by a light source at the macroscopic scale, (b) an infinitesimal volume at the microscopic scale used to derive the modified RTE, and relevant light–matter interactions at (c) the luminophore particle scale, and (d) the luminophore molecular scale using Jablonski diagram. The circled numbers represent: ① light reflection at the top surface, ② light transmission through the bottom surface, ③ QY loss, ④ escape cone loss, ⑤ light collection at edges due to TIR by the waveguide, ⑥ light absorption by the waveguide, ⑦ light absorption and ⑧ light scattering by the luminophore particles, and ⑨ PL emission from the luminophore particles.

The following assumptions are made: (i) the LSC is treated as a homogeneous medium with luminophores being uniformly distributed within the waveguide matrix; (ii) the LSC medium is stationary, non-polarizing, and at local thermodynamic equilibrium [11], justifying the quasi-steady radiative transfer treatment in the LSC; (iii) light is only scattered by the luminophore particles in an elastic manner, and light scattering by the waveguide matrix is hence not considered; (iv) PL emission from the luminophore is assumed isotropic, a typical treatment made in literature [9, 14]; (v) the characteristic length of the infinitesimal volume (**Fig. 1b**) is assumed much larger than the wavelength of both the incident light and the PL emission such that the laws of geometric optics are valid; (vi) the LSC medium has a constant refractive index, so the light travels through it along straight lines; (vii) the top, bottom and all edge surfaces of the LSC are assumed optically smooth; (viii) the absorptive index of most waveguides (glass, PMMA, di-ureasil) is usually far lower (at least two orders of magnitude) than their refractive index in the AM 1.5 standard spectrum [15, 16], such that light reflection and refraction at the waveguide–air interface can be modelled via Snell’s law and Fresnel’s relation; (ix) all edge surfaces are treated as perfect absorber; (x) the LSC is assumed a cold medium, so blackbody intensity at the medium temperature is neglected; and (xi) the luminophore particles are of uniform size and shape, so particle size effects are not considered.

## 2.1 Modified radiative transfer equation

Attenuation by absorption and out-scattering. Similar to the phenomena involved in deriving the conventional RTE, the spectral light intensity in the LSC can be attenuated due to light absorption by the waveguide, as well as light absorption and out-scattering (assumption (iii)) by the luminophore particles:

$$\left. \frac{dI_\lambda(\vec{r}, \hat{s})}{|d\vec{s}|} \right|_{\text{attenuated}} = -(\kappa_{\lambda, \text{wg}} + \kappa_{\lambda, \text{p}} + \sigma_{\text{s}\lambda, \text{p}}) I_\lambda(\vec{r}, \hat{s}) \quad (1)$$

where  $\kappa_{\lambda, \text{wg}}$ ,  $\kappa_{\lambda, \text{p}}$ , and  $\sigma_{\text{s}\lambda, \text{p}}$  are the spectral absorption coefficient of the waveguide, the spectral absorption and scattering coefficients of the luminophore particles, respectively. The determination of these coefficients will be discussed in **Section 2.2**.

Augmentation by in-scattering and PL emission. Different from the conventional RTE applied to cold media (assumption (x)) where beam augmentation purely comes from light in-scattering, a new contribution in the LSC is the PL emission from the luminophore particles:

$$\begin{aligned} \left. \frac{dI_\lambda(\vec{r}, \hat{s})}{|d\vec{s}|} \right|_{\text{augmented}} &= \frac{\sigma_{\text{s}\lambda, \text{p}}}{4\pi} \int_{4\pi} I_\lambda(\vec{r}, \hat{s}') \Phi_{\text{s}\lambda, \text{p}}(\hat{s}', \hat{s}) d\Omega' \\ &+ \frac{1}{4\pi} \int_{4\pi} \int_{\lambda_{\text{abs}, \text{min}}}^{\lambda_{\text{abs}, \text{max}}} \kappa_{\lambda, \text{p}}(\lambda_{\text{abs}}) I_\lambda(\lambda_{\text{abs}}, \vec{r}, \hat{s}'') \cdot \phi_{\text{PL}} \frac{\lambda_{\text{abs}}}{\lambda} d\lambda_{\text{abs}} \cdot P_{\text{PL}\lambda, \text{p}}(\lambda) \cdot \Phi_{\text{PL}\lambda, \text{p}}(\hat{s}'', \hat{s}) d\Omega'' \end{aligned} \quad (2)$$

where  $\Phi_{\text{s}\lambda, \text{p}}$ ,  $\phi_{\text{PL}}$ ,  $P_{\text{PL}\lambda, \text{p}}$  and  $\Phi_{\text{PL}\lambda, \text{p}}$  are the scattering phase function, the photoluminescence quantum yield (PLQY), the PL wavelength function, and the PL phase function of the luminophore particles, respectively. The dummy symbols of  $\Omega'$  and  $\Omega''$  denote the incoming solid angles. The first term on the right-hand side (RHS) of Eq. (2) is the rate of light in-scattering by the luminophore particles from all other incoming directions  $\hat{s}'$  into the propagation direction  $\hat{s}$ ; while the second term on the RHS represents the rate of PL emission after absorbing all incoming photons from all directions  $\hat{s}''$  within the range of absorption spectrum  $\lambda_{\text{abs}}$ . The PLQY in Eq. (2) is a quantum-based property defined as the ratio of the PL emitted photons to the absorbed ones per unit time,  $\phi_{\text{PL}} = \dot{N}_\lambda / \dot{N}_{\lambda, \text{abs}}$ . Due to the non-radiative decay effect such as luminescence quenching, not every photon that is absorbed by the luminophore will be emitted via PL, leading to non-unity PLQY. The combined term  $\phi_{\text{PL}} \cdot \lambda_{\text{abs}} / \lambda$  in Eq. (2) serves to account for the energy difference between the absorbed intensity and the PL emission intensity due to Stokes shift effect:

$$\frac{I_\lambda}{I_{\lambda, \text{abs}}} = \frac{\dot{N}_\lambda \cdot h\nu}{\dot{N}_{\lambda, \text{abs}} \cdot h\nu_{\text{abs}}} = \frac{\dot{N}_\lambda}{\dot{N}_{\lambda, \text{abs}}} \frac{\lambda_{\text{abs}}}{\lambda} = \phi_{\text{PL}} \frac{\lambda_{\text{abs}}}{\lambda} \quad (3)$$

The PL wavelength function  $P_{\text{PL}\lambda, \text{p}}(\lambda)$  appearing in Eq. (2) describes the probability that a photon will be emitted at wavelength  $\lambda$  via PL. It is assumed independent from the absorbed wavelength, because PL emission usually occurs from the lowest excited electronic state regardless of the vibrational level of the excited electron state after photon absorption, a phenomenon known as Kasha's rule [17]. Consequently, the following relation will be automatically satisfied:

$$\int_{\lambda_{\text{PL}, \text{min}}}^{\lambda_{\text{PL}, \text{max}}} P_{\text{PL}\lambda, \text{p}}(\lambda) d\lambda = 1 \quad (4)$$

The PL wavelength function  $P_{\text{PL}\lambda, \text{p}}$  is a unique characteristic of the specific luminophore material, and can be obtained from its normalized emission spectrum intensity.

Finally, the PL phase function  $\Phi_{\text{PL}\lambda,\text{p}}$  in Eq. (2) describes the probability that an absorbed photon coming from one direction  $\hat{s}''$  will be emitted via PL into direction  $\hat{s}$ , and follows a similar definition to the scattering phase function:

$$\frac{1}{4\pi} \int_{4\pi} \Phi_{\text{PL}\lambda,\text{p}}(\hat{s}'', \hat{s}) d\Omega = 1 \quad (5)$$

where  $\Omega$  represents the outgoing solid angle. For isotropic PL emission (assumption (iv)), we have  $\Phi_{\text{PL}\lambda,\text{p}}(\hat{s}'', \hat{s}) = 1$ . The determination of  $\Phi_{\text{PL}\lambda,\text{p}}$ ,  $\phi_{\text{PL}}$  and  $P_{\text{PL}\lambda,\text{p}}$  will be described in **Section 2.2**.

**Radiative energy balance.** The change in spectral intensity in the LSC is found by summing up all contributions, Eqs. (1) and (2), leading to the following modified RTE:

$$\begin{aligned} \hat{s} \cdot \nabla I_{\lambda}(\vec{r}, \hat{s}) = & -(\kappa_{\lambda,\text{wg}} + \kappa_{\lambda,\text{p}} + \sigma_{\text{s}\lambda,\text{p}}) I_{\lambda}(\vec{r}, \hat{s}) + \frac{\sigma_{\text{s}\lambda,\text{p}}}{4\pi} \int_{4\pi} I_{\lambda}(\vec{r}, \hat{s}') \Phi_{\text{s}\lambda,\text{p}}(\hat{s}', \hat{s}) d\Omega' \\ & + \frac{1}{4\pi} \frac{\phi_{\text{PL}}}{\lambda} P_{\text{PL}\lambda,\text{p}}(\lambda) \int_{\lambda_{\text{abs},\text{min}}}^{\lambda_{\text{abs},\text{max}}} \kappa_{\lambda,\text{p}}(\lambda_{\text{abs}}) \lambda_{\text{abs}} G_{\lambda}(\lambda_{\text{abs}}, \vec{r}) d\lambda_{\text{abs}} \end{aligned} \quad (6)$$

where we have introduced the spectral incident radiation function  $G_{\lambda} = \int_{4\pi} I_{\lambda}(\vec{r}, \hat{s}'') d\Omega''$ , and exchanged the order of integration over wavelength and solid angle given their independence. Compared with the conventional RTE applicable for participating media in the absence of PL emission [11], the modified RTE, Eq. (6), incorporates a new term at the end of its RHS to account for the PL emission effect, which introduces additional challenge in solving it. In addition, unlike the RTE of LSC in Ref. [6] that treats photon absorption and PL emission independently without the need for PL emission spectrum, our Eq. (6) requires the inputs of absorption and PL emission spectra as well as PLQY. This fundamentally respects that both photon absorption and PLQY should occur simultaneously in order to trigger the PL emission. Failing to capture this fact in Ref. [6] is the source of model inconsistency between its RTE and the total radiative energy balance equation. A similar modified RTE is also found in literature [18-20] for a different application—phosphor-converted light-emitting diodes.

To get the net radiative energy balance within an infinitesimal volume (**Fig. 1b**), Eq. (6) can be integrated over all solid angles, and its final version becomes:

$$\begin{aligned} \nabla \cdot \mathbf{q}_{\lambda,\text{rad}} = & -(\kappa_{\lambda,\text{wg}} + \kappa_{\lambda,\text{p}}) G_{\lambda} \\ & + \frac{\phi_{\text{PL}}}{\lambda} P_{\text{PL}\lambda,\text{p}}(\lambda) \int_{\lambda_{\text{abs},\text{min}}}^{\lambda_{\text{abs},\text{max}}} \kappa_{\lambda,\text{p}}(\lambda_{\text{abs}}) \lambda_{\text{abs}} G_{\lambda}(\lambda_{\text{abs}}, \vec{r}) d\lambda_{\text{abs}} \end{aligned} \quad (7)$$

The divergence of the total radiative heat flux can be further acquired by performing integration over the spectrum for Eq. (7):

$$\nabla \cdot \mathbf{q}_{\text{rad}} = - \int_0^{\infty} \kappa_{\lambda,\text{wg}} G_{\lambda} d\lambda - \left( 1 - \phi_{\text{PL}} \frac{\bar{\lambda}_{\text{abs}}}{\bar{\lambda}_{\text{PL}}} \right) \int_{\lambda_{\text{abs},\text{min}}}^{\lambda_{\text{abs},\text{max}}} \kappa_{\lambda,\text{p}} G_{\lambda} d\lambda \quad (8)$$

where we have introduced the mean absorption and emission spectrum, respectively:

$$\bar{\lambda}_{\text{abs}} = \frac{\int_{\lambda_{\text{abs},\text{min}}}^{\lambda_{\text{abs},\text{max}}} \kappa_{\lambda,\text{p}}(\lambda_{\text{abs}}) \lambda_{\text{abs}} G_{\lambda}(\lambda_{\text{abs}}, \vec{r}) d\lambda_{\text{abs}}}{\int_{\lambda_{\text{abs},\text{min}}}^{\lambda_{\text{abs},\text{max}}} \kappa_{\lambda,\text{p}}(\lambda_{\text{abs}}) G_{\lambda}(\lambda_{\text{abs}}, \vec{r}) d\lambda_{\text{abs}}} \quad \text{and} \quad \frac{1}{\bar{\lambda}_{\text{PL}}} = \int_{\lambda_{\text{PL},\text{min}}}^{\lambda_{\text{PL},\text{max}}} \frac{1}{\lambda} P_{\text{PL}\lambda,\text{p}}(\lambda) d\lambda.$$

Equation (8) states that the net radiative energy loss within an infinitesimal volume is equal to the absorbed radiation by the waveguide plus the radiation loss from the luminophore due to the change in wavelength between

absorption and PL emission spectra. Different from the self-inconsistent thermodynamic model developed in Refs [3, 5, 6], our modified RTE (Eq. (6)) and the total radiative energy balance equation (Eq. (8)) here are mutually consistent without additional input.

## 2.2 Determination of photophysical properties

The photophysical properties appearing in Eq. (6) can be determined using combined theoretical and experimental techniques. The absorption coefficient of the waveguide matrix  $\kappa_{\lambda,\text{wg}}$  is a purely material-dependent property, and can be readily determined from the electromagnetic theory [21]:

$$\kappa_{\lambda,\text{wg}} = \frac{4\pi k_{\lambda,\text{wg}}}{\lambda_0} \quad (9)$$

where  $k_{\lambda,\text{wg}}$  and  $\lambda_0$  are the absorptive index of the waveguide and the wavelength of the light in vacuum. Alternatively, one can refer to the UV–Vis spectroscopy technique to measure both the spectral reflectivity  $R_{\lambda,\text{wg}}$  and transmissivity  $T_{\lambda,\text{wg}}$  of the waveguide based on the following relation:

$$\kappa_{\lambda,\text{wg}} = -\frac{1}{H_{\text{wg}}} \ln\left(\frac{T_{\lambda,\text{wg}}}{1-R_{\lambda,\text{wg}}}\right) \quad (10)$$

where  $H_{\text{wg}}$  is the thickness of the waveguide sample.

The properties of the luminophore particles ( $\kappa_{\lambda,\text{p}}$ ,  $\sigma_{s\lambda,\text{p}}$  and  $\Phi_{s\lambda,\text{p}}$ ) depend not only on the material type, but also on their concentration and shape. When the luminophore concentration is low, the clearance between particles will be large enough that independent scattering can be assumed [11], leading to the following relation for uniform luminophore particle size (assumption (xi)):

$$\kappa_{\lambda,\text{p}} = N_{\text{p}} C_{\text{abs,p}} \quad (11)$$

$$\sigma_{s\lambda,\text{p}} = N_{\text{p}} C_{\text{sca,p}} \quad (12)$$

$$\Phi_{s\lambda,\text{p}}(\hat{s}', \hat{s}) = \Phi_{\text{sca,p}}(\hat{s}', \hat{s}) \quad (13)$$

where  $N_{\text{p}}$ ,  $C_{\text{abs,p}}$ ,  $C_{\text{sca,p}}$ , and  $\Phi_{\text{sca,p}}$  are the luminophore particle number density, the absorption cross section, the scattering cross section, and the scattering phase function of a single particle, respectively. The determination of the particle-level properties of  $C_{\text{abs,p}}$ ,  $C_{\text{sca,p}}$  and  $\Phi_{\text{sca,p}}$  can refer to one of the two modelling approaches depending on the particle shape: (i) Lorenz–Mie theory for spherical particles [11, 21], and (ii) discrete dipole approximation for non-spherical particles of arbitrary shape [22]. Both approaches require the knowledge of the complex refractive index of the luminophore material, which can be predicted by classical theories [21] or measured experimentally [23]. When the luminophore concentration is so high that independent scattering becomes invalid, the properties of  $\kappa_{\lambda,\text{p}}$ ,  $\sigma_{s\lambda,\text{p}}$  and  $\Phi_{s\lambda,\text{p}}$  can be determined either theoretically [24, 25] or experimentally [14]. On the other hand, if the complex refractive index of the luminophore material is simply not available, one needs to rely on experimental techniques [14] to determine these properties, regardless of the luminophore concentration and particle shape in the LSC.

Finally, the PLQY  $\phi_{\text{PL}}$ , and PL wavelength function  $P_{\text{PL}\lambda,\text{p}}(\lambda)$  of the luminophore can be determined experimentally using a fluorometer–integrating sphere setup [26] and a fluorometer [27], respectively.

### 2.3 Boundary conditions

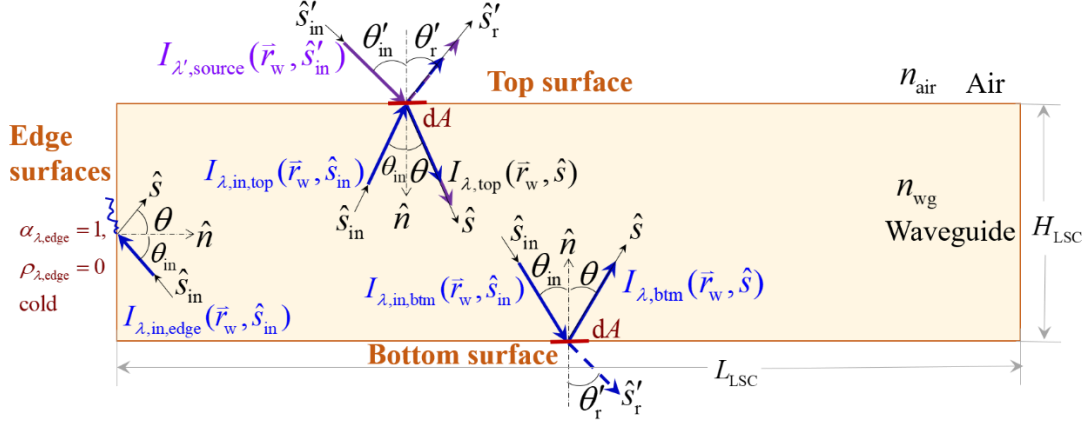


**Fig. 2.** Schematic of the outgoing ( $\hat{n} \cdot \hat{s} > 0$ ) spectral intensity specified at each boundary surface of the LSC (front view of **Fig. 1a**, not to scale).

The modified RTE, Eq. (6), is a steady-state, first-order differential equation for the spectral intensity in an arbitrary direction  $\hat{s}$ , so only one boundary condition is required for each direction in order to solve it. The spectral intensity leaving a wall into direction  $\hat{s}$  will be specified in the following.

For the top surface, the outgoing intensity towards the waveguide is composed of both the refracted intensity of the incident light from air to waveguide and the reflected intensity within the waveguide itself (see **Fig. 2**). The refracted intensity  $I_{\lambda,\text{refract}}(\vec{r}_w, \hat{s}(\theta))$  can be calculated based on radiative energy balance:

$$(1 - \rho_{\lambda,\text{top,air}}(\theta'_{\text{in}}, \theta'_r)) \cdot I'_{\lambda,\text{source}}(\vec{r}_w, \hat{s}'(\theta'_{\text{in}})) \cdot (dA \cos \theta'_{\text{in}}) d\Omega' d\lambda' dt = I_{\lambda,\text{refract}}(\vec{r}_w, \hat{s}(\theta)) (dA \cos \theta) d\Omega d\lambda dt \quad (14)$$

where  $I'_{\lambda,\text{source}}$  is the external spectral intensity incident on the top surface of LSC. For collimated irradiation impinged onto the LSC in the direction of  $\hat{s}'_{\text{in}}$ , we have:

$$I'_{\lambda,\text{source}} = q''_{\lambda',\text{source}} \delta(\hat{s} - \hat{s}'_{\text{in}}) \quad (15)$$

where  $q''_{\lambda',\text{source}}$  is the radiative flux of the light source, and  $\delta$  is the Dirac delta function defined as:

$$\delta(x) = \begin{cases} 0, & |x| \geq \varepsilon \\ \lim_{\varepsilon \rightarrow 0} \frac{1}{2\varepsilon}, & |x| < \varepsilon \end{cases} \quad (16)$$

The solid angle in Eq. (14) can be eliminated using  $d\Omega' = \sin \theta'_{\text{in}} d\theta'_{\text{in}} d\varphi$  and  $d\Omega = \sin \theta d\theta d\varphi$  (the azimuthal angle  $\varphi$  does not change when light passes from air to waveguide). Introducing the Snell's law (assumption (viii)) and its differential version,  $n_{\text{air}} \sin \theta'_{\text{in}} = n_{\text{wg}} \sin \theta$ ,  $n_{\text{air}} \cos \theta'_{\text{in}} d\theta'_{\text{in}} = n_{\text{wg}} \cos \theta d\theta$ , along with the differential version of the wavelength relation  $n_{\text{air}} d\lambda' = n_{\text{wg}} d\lambda$ , Eq. (14) is simplified to:

$$I_{\lambda,\text{refract}}(\vec{r}_w, \hat{s}(\theta)) = (1 - \rho_{\lambda,\text{top,air}}(\theta'_{\text{in}}, \theta'_r)) \cdot I'_{\lambda',\text{source}}(\vec{r}_w, \hat{s}'(\theta'_{\text{in}})) \cdot \left( \frac{n_{\text{wg}}}{n_{\text{air}}} \right)^3 \quad (17)$$

Consequently, the boundary condition at the top surface is:

$$\begin{aligned}
I_{\lambda,\text{top}}(\vec{r}_w, \hat{s}(\theta))\Big|_{\hat{s}\cdot\hat{n}>0} &= I_{\lambda,\text{refract}}(\vec{r}_w, \hat{s}(\theta)) + I_{\lambda,\text{reflect}}(\vec{r}_w, \hat{s}(\theta)) \\
&= (1 - \rho_{\lambda,\text{top,air}}(\theta'_\text{in}, \theta'_\text{r})) \cdot I_{\lambda',\text{source}}(\vec{r}_w, \hat{s}'(\theta'_\text{in})) \cdot \left(\frac{n_{\text{wg}}}{n_{\text{air}}}\right)^3 + \rho_{\lambda,\text{top,wg}}(\theta_\text{in}, \theta) \cdot I_{\lambda,\text{in,top}}(\vec{r}_w, \hat{s}_\text{in}(\theta_\text{in}))
\end{aligned} \tag{18}$$

where  $I_{\lambda,\text{in,top}}$  is the internal spectral intensity incident on the top surface within the waveguide.

In terms of the bottom surface, the outgoing spectral intensity is composed of self-reflected intensity only (see **Fig. 2**):

$$I_{\lambda,\text{btm}}(\vec{r}_w, \hat{s})\Big|_{\hat{s}\cdot\hat{n}>0} = \rho_{\lambda,\text{btm,wg}}(\theta_\text{in}, \theta) \cdot I_{\lambda,\text{in,btm}}(\vec{r}_w, \hat{s}_\text{in}(\theta_\text{in})) \tag{19}$$

The bi-directional spectral specular reflectivity terms ( $\rho_{\lambda,\text{top,air}}$ ,  $\rho_{\lambda,\text{top,wg}}$  and  $\rho_{\lambda,\text{btm,wg}}$ ) appearing in Eqs. (14), (17)–(19) can be readily determined from Fresnel's relation [11] (assumption (viii)):

$$\rho_{\lambda,\text{top,air}} = \frac{1}{2} \left[ \left( \frac{\cos \theta - n_{\text{wg}} \cos \theta'_\text{in}}{\cos \theta + n_{\text{wg}} \cos \theta'_\text{in}} \right)^2 + \left( \frac{\cos \theta'_\text{in} - n_{\text{wg}} \cos \theta}{\cos \theta'_\text{in} + n_{\text{wg}} \cos \theta} \right)^2 \right] \tag{20}$$

$$\rho_{\lambda,\text{btm,wg}} = \rho_{\lambda,\text{top,wg}} = \begin{cases} \frac{1}{2} \left[ \left( \frac{n_{\text{wg}} \cos \theta'_\text{r} - \cos \theta_\text{in}}{n_{\text{wg}} \cos \theta'_\text{r} + \cos \theta_\text{in}} \right)^2 + \left( \frac{\cos \theta'_\text{r} - n_{\text{wg}} \cos \theta_\text{in}}{\cos \theta'_\text{r} + n_{\text{wg}} \cos \theta_\text{in}} \right)^2 \right], & \theta_\text{in} < \sin^{-1}(1/n_{\text{wg}}) \\ 1, & \theta_\text{in} \geq \sin^{-1}(1/n_{\text{wg}}). \end{cases} \tag{21}$$

Finally, for the edge surfaces, the assumptions of perfect absorber (assumption (ix)) and cold medium (assumption (x)) lead to the following boundary condition (see **Fig. 2**):

$$I_{\lambda,\text{edge}}(\vec{r}_w, \hat{s})\Big|_{\hat{s}\cdot\hat{n}>0} = 0 \tag{22}$$

## 2.4 Solution via Monte Carlo method

Given that the modified RTE (Eq. (6)) for the LSC is a complicated integral–differential equation as a function of location, direction and wavelength, solving it using conventional numerical techniques (finite volume method, spherical harmonics method, zonal method, etc.) would become extremely difficult. On the other hand, such a problem can be readily solved by the MC method in which the history of a large number of photons is traced and spectrally resolved to any degree of accuracy [9, 28].

## 2.5 Performance metrics

The key performance metrics for the LSC as a photonic device are the internal and external photon efficiencies following the protocols proposed in Ref. [29]:

$$\eta_{\text{int}} = \frac{\sum_{i=1}^4 \sum_{\lambda} \dot{N}_{\lambda,\text{edge},i}}{\sum_{\lambda} \dot{N}_{\lambda,\text{abs}}} = \frac{\sum_{i=1}^4 \int_{A_{\text{edge}}} \int_{4\pi} \int_{\lambda} I_{\lambda,\text{edge},i}(\lambda, \hat{s}_\text{in}) \frac{\lambda}{hc} d\lambda \cdot d\Omega_\text{in} \cdot |\hat{n} \cdot \hat{s}_\text{in}| dA}{\int_{A_{\text{top}}} \int_{4\pi} \int_{\lambda} I_{\lambda,\text{refract,top}}(\lambda, \hat{s}) \cdot (1 - 10^{-(\kappa_{\lambda,p} + \sigma_{\text{s}\lambda,p})H_{\text{LSC}}}) \cdot \frac{\lambda}{hc} d\lambda \cdot d\Omega \cdot |\hat{n} \cdot \hat{s}| dA} \tag{23}$$

$$\eta_{\text{ext}} = \frac{\sum_{i=1}^4 \sum_{\lambda} \dot{N}_{\lambda,\text{edge},i}}{\sum_{\lambda} \dot{N}_{\lambda,\text{in}}} = \frac{\sum_{i=1}^4 \int_{A_{\text{edge}}} \int_{4\pi} \int_{\lambda} I_{\lambda,\text{edge},i}(\lambda, \hat{s}_\text{in}) \frac{\lambda}{hc} d\lambda \cdot d\Omega_\text{in} \cdot |\hat{n} \cdot \hat{s}_\text{in}| dA}{\int_{A_{\text{top}}} \int_{4\pi} \int_{\lambda'} I_{\lambda',\text{source}}(\lambda', \hat{s}) \cdot \frac{\lambda'}{hc} d\lambda' \cdot d\Omega \cdot |\hat{n} \cdot \hat{s}| dA} \tag{24}$$

where  $\dot{N}_{\lambda,\text{edge},i}$ ,  $\dot{N}_{\lambda,\text{abs}}$ , and  $\dot{N}_{\lambda,\text{in}}$  are the spectral photon rates collected at edge  $i$ , absorbed by the LSC, and incident on the LSC, respectively. The internal photon efficiency is a measure of the quality of

light transport process after photon absorption, which is independent of both the light source and absorption spectra. While on the other hand, the external photon efficiency captures the whole light transport process and is more relevant for evaluating the commercial viability of an LSC.

### 3. Application to LSCs doped with Lumogen F Red 305

The modelling framework described above is applied to investigate the LSCs composed of PMMA as the waveguide matrix doped with a commercial organic dye LFR305, the benchmark luminophore widely employed in the field of LSC [16, 30, 31]. Nonetheless, most of the LFR305 based LSCs are in the form of thin-film type [31, 32] and are often investigated together with photovoltaic cells for electricity generation [33]. Very few efforts have been made to study its doped counterpart and to treat it as an independent photonic device. In addition, there is a lack of systematic studies on the impact of both the waveguide and luminophore properties in order to analyze different loss mechanisms [16, 26, 34], which is crucial for designing efficient LSCs.

#### 3.1 Photophysical properties

Unlike other types of luminophore such as inorganic phosphors [9, 35] or quantum dots [36] that are essentially scattering, the LFR305 is a non-scattering organic dye, so both the scattering coefficient and scattering phase function in Eq. (6) become zero:  $\sigma_{s,\lambda,p} = \Phi_{s,\lambda,p} = 0$ . The remaining photophysical properties of the LFR305 doped in PMMA can be determined following the approach described in section 2.2, and are found available from literature [8, 26, 37] as shown in **Fig. 3**. Note that the absorption coefficient of LFR305 in **Fig. 3b** is the spectral molar absorption coefficient  $\varepsilon_{\lambda,p}$ , and its relation to the spectral absorption coefficient  $\kappa_{\lambda,p}$  is given by [37]:

$$\varepsilon_p = \frac{\kappa_{\lambda,p}}{c_p} \log_{10} e \quad (25)$$

where  $c_p$  is the molar concentration of luminophore particles assuming that Beer–Lambert law is valid within the range of LFR305 concentration (see **Table 1**). It is obvious that the absorption spectrum of PMMA mainly lies in 300–400 nm, while that of LFR305 extends towards the visible spectrum of up to 620 nm, so competition in light absorption between PMMA and LFR305 occurs in the UV range only. The PL emission spectrum of LFR305 is roughly in the range of 570–800 nm, and an overlap of 570–620 nm exists between its absorption and emission spectrum, leading to PL re-absorption for downstream light transport process. Note there is a red shift in the peak intensity between the absorption and emission spectrum  $\Delta\lambda_s$ , a phenomenon known as Stokes shift, and its effect will be investigated hypothetically in section 3.3.2. The PLQY of LSCs doped with LFR305 is found independent of the excitation wavelength [26], and decreases linearly with the dye concentration but always stays above 93% when LFR305 concentration is below  $2 \times 10^{-4}$  mol/L.

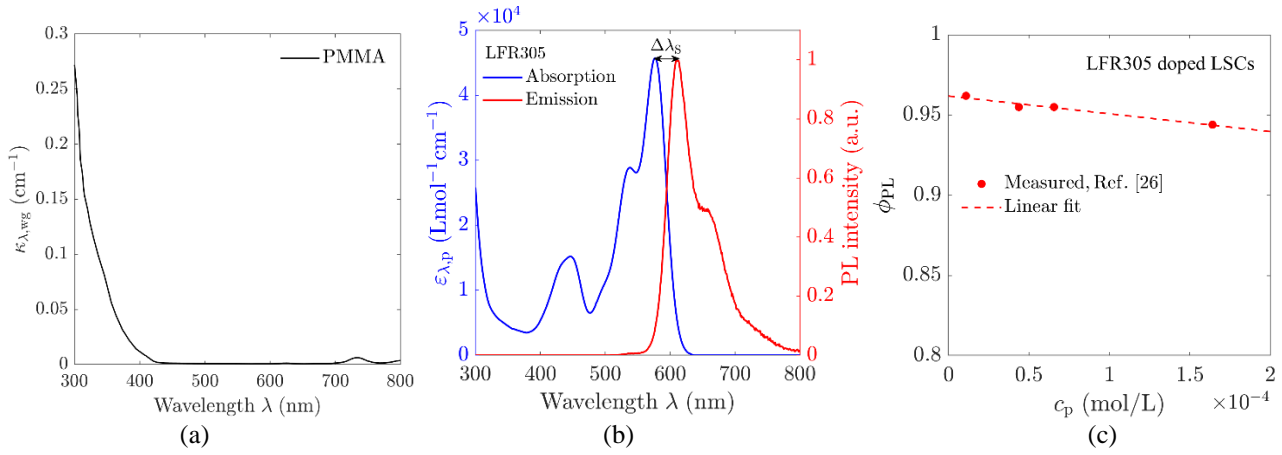


**Fig. 3.** Photophysical properties of LSCs composed of PMMA doped with varying concentrations of LFR305 dye: (a) spectral absorption coefficient of PMMA from Wilson [37], (b) spectral molar absorption coefficient (left y-axis) and normalized PL emission spectrum (right y-axis) of LFR305 from Zhang et al. [8], and (c) PLQY at varying LFR305 concentrations from Tummeltshammer et al. [26].

### 3.2 Numerical solution and validation

Once the photophysical properties are available, Eq. (6) along with its boundary conditions (Eqs. (18)–(22)) can be readily solved using the MC ray tracing approach. Here, we only consider the scenario where the light source is normally incident on the LSC ( $\theta'_n = 0^\circ$ ) in order to explore the LSC performance under varying design and material choices. Readers are referred to Ref. [38] for the effect of light incident angle. A number of open-source MC codes are available in literature [8, 9, 39, 40], and the one developed by Zhang et al. [8] is adopted here with modifications including: (i) instead of the AM 1.5 standard solar spectral irradiance (**Fig. S1a**), its spectral photon flux (see **Fig. S1b**) will be used as the light source in order to be consistent with the quantum nature of the performance metrics as defined in section 2.5, and (ii) light losses via top reflection and bottom transmission are further distinguished to quantify different loss mechanisms. A flowchart describing the MC ray tracing process can be found in **Fig. S2**. For each simulation, a ray number independence check is needed to warrant sufficient confidence in the result, and an example for the baseline case (see **Table 1**) is put in **Table S1**. To validate the MC ray tracing model, the experimental data of LSCs doped with Coumarin 6 at varying dye concentrations reported by Tummeltshammer et al. [26] are used, and good agreement is achieved between measurement and simulation as shown in **Fig. S3**.

### 3.3 Performance analysis

The key model parameters used for the MC ray tracing simulation are summarized in **Table 1** which includes both the baseline and parametric scenarios. The baseline case is a square shaped LSC ( $L_{\text{LSC}} = W_{\text{LSC}}$ ) with dimensions of 10 cm × 10 cm × 5 mm composed of PMMA as the waveguide with a spectral average refractive index of 1.49 doped with LFR305 dye at a concentration of  $1 \times 10^{-4}$  mol L<sup>-1</sup> with 95% PLQY. The parametric case is aimed to examine the effects of certain geometric and material parameters, under both realistic and hypothetical scenarios. The realistic scenarios consider the effects of LSC length and thickness, as well as the molar concentration of LFR305, while the hypothetical scenarios assume different material properties, such as the waveguide refractive index, the PLQY of the luminophore particles, and the Stokes shift. Note that the parametric study will be conducted by varying the variable of interest within its range while keeping all other parameters constant at their baseline values, unless stated otherwise.

**Table 1.** Summary of model parameters for MC ray tracing simulation

| Parameter                | Baseline value     | Parametric values                       | Unit  |
|--------------------------|--------------------|---|-------|
| $L_{LSC}$                | 10                 | 5–25                                    | cm    |
| $H_{LSC}$                | 5                  | 2–10                                    | mm    |
| $c_p$                    | $1 \times 10^{-4}$ | $1 \times 10^{-5}$ – $2 \times 10^{-4}$ | mol/L |
| $n_{wg,hypo}$            | 1.49               | 1.1–2.1                                 | –     |
| $\phi_{PL,hypo}$         | 0.95               | 0.5–0.99                                | –     |
| $\Delta\lambda_{s,hypo}$ | 33                 | 0–100                                   | nm    |

### 3.3.1 Realistic scenarios

**Baseline scenario.** Fig. 4 displays the baseline performance for both external and internal photon fates. Among all external loss mechanisms, transmission loss is the dominating pathway (79.4%), followed by the escape cone loss (4.8%) and the top reflection loss (3.9%). This is mainly due to the low fraction of the LFR305 absorption spectrum (300–620 nm) within the broadband solar spectrum (300–4000 nm) and also to the non-scattering nature of LFR305, leaving most sunlight, particularly those outside the LFR305 absorption spectrum, directly lost via bottom transmission. The QY loss is the lowest (1.2%) mainly due to the high value of PLQY (0.95). Consequently, an external photon efficiency of 10.6% is predicted for the baseline LSC. The escape cone loss dominates over the QY loss (28.9% vs 7.2%) among the internal photon fates after light absorption, a result of the PMMA refractive index of 1.49 and high PLQY of 0.95. The internal photon efficiency is 63.8%.

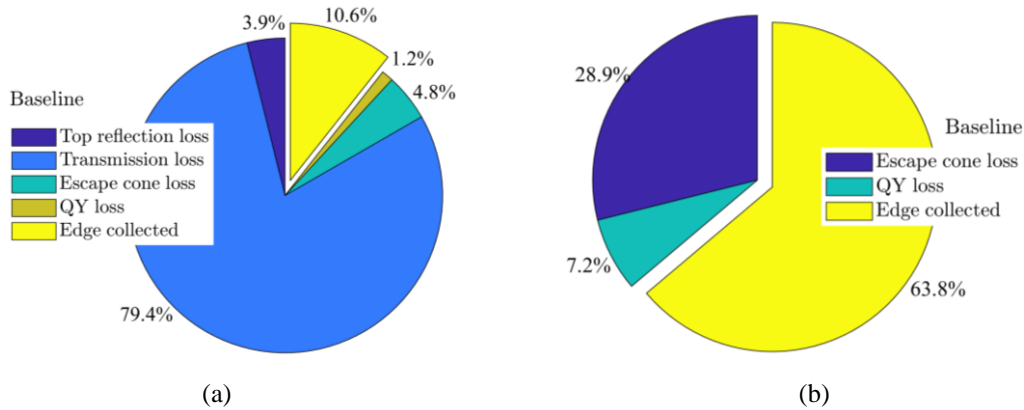


**Fig. 4.** LSC baseline performance in terms of (a) external photon fate, and (b) internal photon fate.

**Effect of geometric parameters.** The effect of LSC length is shown in Fig. 5 for both the external and internal light transport processes while holding other parameters unchanged at their baseline values. Given the constant contribution from the top reflection loss (3.9%) and the transmission loss (79.5%) as shown in Fig. 5a, a minor decrease of 6% is observed for the external photon efficiency as the LSC length increases, from 11.0% at a length of 5 cm to 10.3% at a length of 25 cm. This indicates that the performance of a lab-scale LSC can be roughly maintained for a pilot-scale device, implying good scale-up potential that is crucial for future commercial deployment. As to the internal transport process (Fig. 5b), a larger LSC represents longer light transport path that will trigger more PL re-absorption events by downstream LFR305 particles, leading to both higher escape cone loss and QY loss. Consequently, the internal photon efficiency decreases monotonically with higher  $L_{LSC}$ , from 65.9% at 5 cm length to 62.0% at 25 cm.

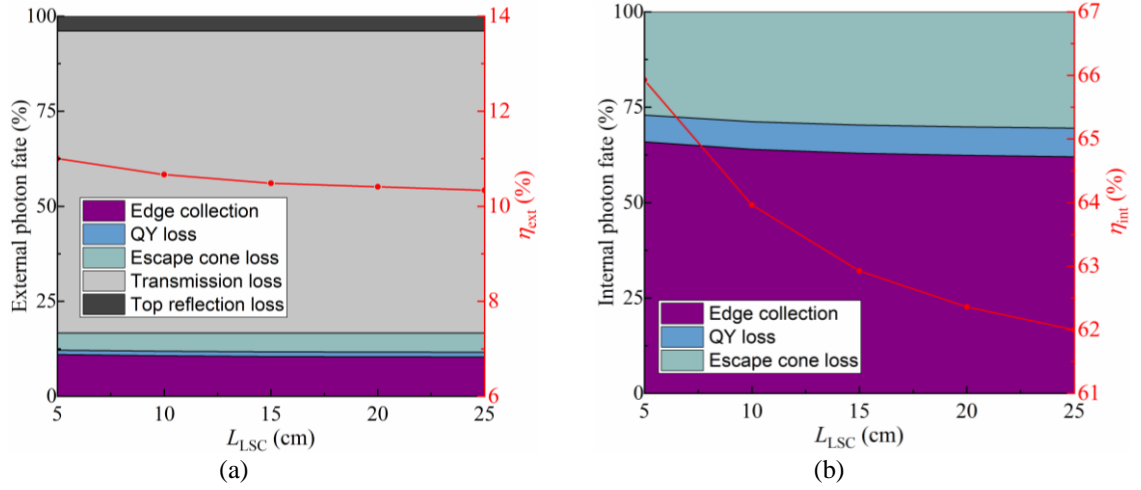


**Fig. 5.** Effect of LSC length on: (a) external photon fate (left y-axis) and external photon efficiency (right y-axis), and (b) internal photon fate (left y-axis) and internal photon efficiency (right y-axis) of LFR305 doped LSCs. Other parameters are kept constant at their baseline values as listed in **Table 1**.

**Fig. 6** illustrates the effect of LSC thickness on its performance. For the external light transport process (**Fig. 6a**), higher LSC thickness signifies longer path along the light incidence direction, leading to enhanced light absorption and hence a decreased transmission loss from 85.1% at 2 mm thickness to 76.2% at 10 mm thickness. Consequently, more photons will be PL emitted and guided to the edges via TIR, though the escape cone loss and QY loss also increases slightly. This results in a 90% increase in external photon efficiency from 6.8% to 13.1%. As to the internal photon transport process (**Fig. 6b**), a sublinear increase trend is found for  $\eta_{int}$  as the LSC becomes thicker, mainly due to the drop in escape cone loss fraction—from 30.7% to 27.0%—among the absorbed photons. The highest  $\eta_{int}$  of 65.6% is achieved at a thickness of 10 mm.

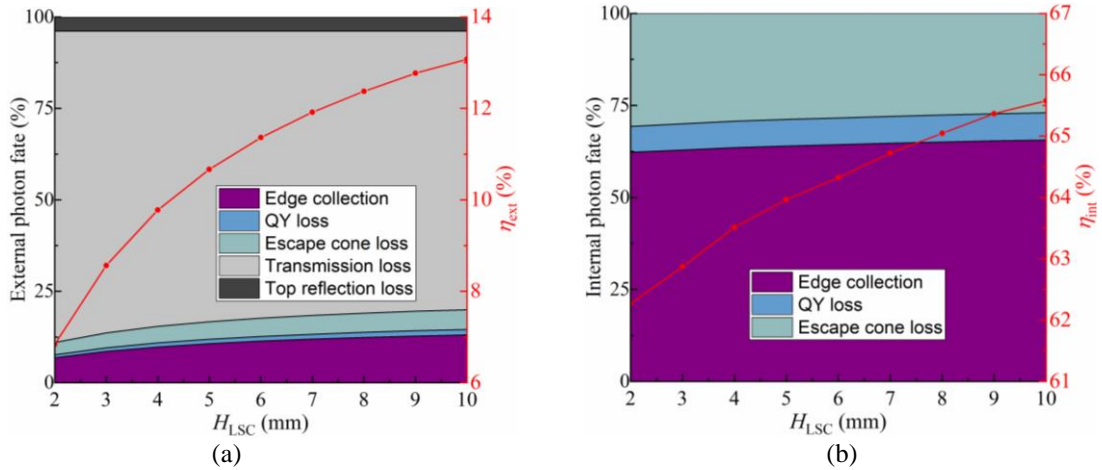


**Fig. 6.** Effect of LSC height on: (a) external photon fate (left y-axis) and external photon efficiency (right y-axis), and (b) internal photon fate (left y-axis) and internal photon efficiency (right y-axis) of LFR305 doped LSCs. Other parameters are kept at their baseline values as listed in **Table 1**.

**Effect of dye concentration.** **Fig. 7a** displays the normalized photon intensity collected at the edges at varying LFR305 concentration versus front-face PL emission (see **Fig. 3b**). It is obvious that the edge photon spectrum resembles the front-face PL emission, confirming light transport via TIR by the waveguide of the PL emission from LFR305 towards the edges. As the dye concentration increases, the edge photon spectrum become red-shifted in comparison to the front-face PL spectrum, from 12 nm at  $1 \times 10^{-5}$  mol/L to 27 nm at  $2 \times 10^{-4}$  mol/L. This is due to the re-absorption effect by downstream LFR305 particles as mentioned earlier. The external photon efficiency (right y-axis)

along with the fractional photon fate (left y-axis) is shown in **Fig. 7b** to reveal different loss mechanisms. Dye concentration mainly affects the external process through influencing the transmission loss. Higher dye concentration leads to higher sunlight absorption, thus lower transmission loss given the constant reflection loss at the top surface (3.87%). Consequently, more photons will be PL emitted and transported towards the edges via TIR, despite the accompanied higher escape cone and QY losses, leading to sublinear increase in the external photon efficiency. The best performance is achieved at the highest dye concentration of  $2 \times 10^{-4}$  mol/L with an external photon efficiency of 12.5%. For the internal transport process after light absorption (**Fig. 7c**),  $\eta_{\text{int}}$  is found to decrease monotonically as LFR305 concentration increases—from 66.2% at  $1 \times 10^{-5}$  mol/L to 62.8% at  $2 \times 10^{-4}$  mol/L, mainly due to the enhanced QY loss as a result of the QY drop at higher  $c_p$  (see **Fig. 3c**). A similar trend in  $\eta_{\text{int}}$  is also reported for thin-film LSCs based on LFR305 [32]. Given the opposite trends observed in the external and internal photon efficiencies, a higher dye concentration is recommended to aim for higher  $\eta_{\text{ext}}$ , since  $\eta_{\text{ext}}$  is a relevant figure of merit for assessing the commercial potential of an LSC.

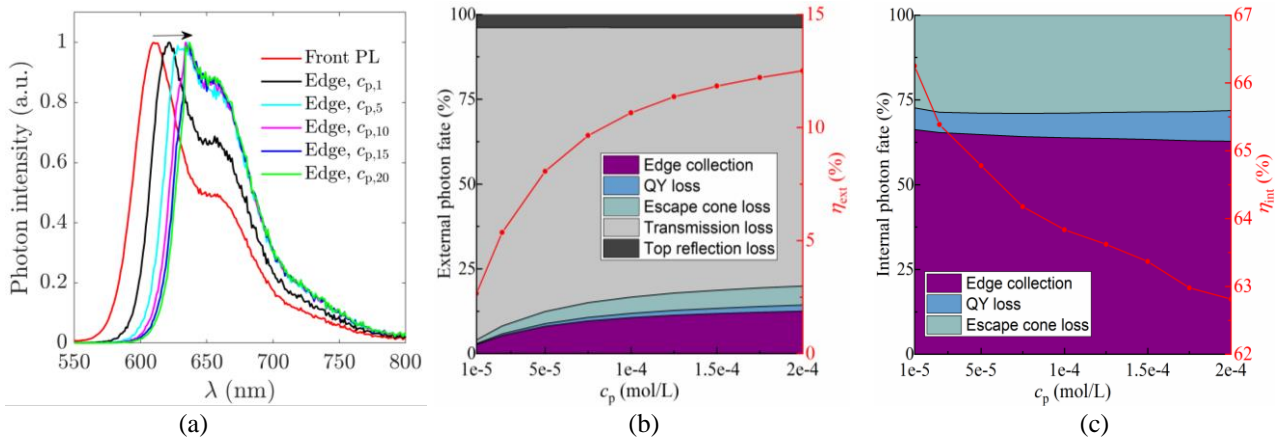


**Fig. 7.** Effect of dye concentration on: (a) normalized photon intensity collected at edges versus front-face PL emission, (b) external photon fate (left y-axis) and external photon efficiency (right y-axis), and (c) internal photon fate (left y-axis) and internal photon efficiency (right y-axis) of LFR305 doped LSCs. Note that  $c_{p,\#}$  in the legend of subfigure (a) represents  $\# \times 10^{-5}$  mol/L, and other parameters are kept at their baseline values as listed in **Table 1**.

### 3.3.2 Hypothetical scenarios

**Effect of waveguide refractive index.** **Fig. 8** illustrates the effect of hypothetical refractive index of the waveguide on LSC performances. As  $n_{\text{wg,hypo}}$  becomes higher, the top reflection loss increases monotonically (see Eq. (20)), but in the meantime, the escape cone loss descends significantly due to the shrink in the critical angle of TIR ( $\sin^{-1}(1/n_{\text{wg,hypo}})$ ), leading to a non-trivial trend in the external photon efficiency as observed in **Fig. 8a**. The best performance is achieved with an  $\eta_{\text{ext}}$  of 11.9% at a medium  $n_{\text{wg,hypo}}$  of around 2.1, which well balances the competing effect between high escape cone loss at low  $n_{\text{wg,hypo}}$  and high top reflection loss at high  $n_{\text{wg,hypo}}$ . By contrast, the internal photon efficiency is found to increase sub-linearly with higher refractive index, from 35.0% when setting  $n_{\text{wg,hypo}}$  at 1.1 to 86.7% at 3.3, mainly due to the substantial drop in the escape cone loss that dominates over the slight increase in the QY loss (**Fig. 8b**).

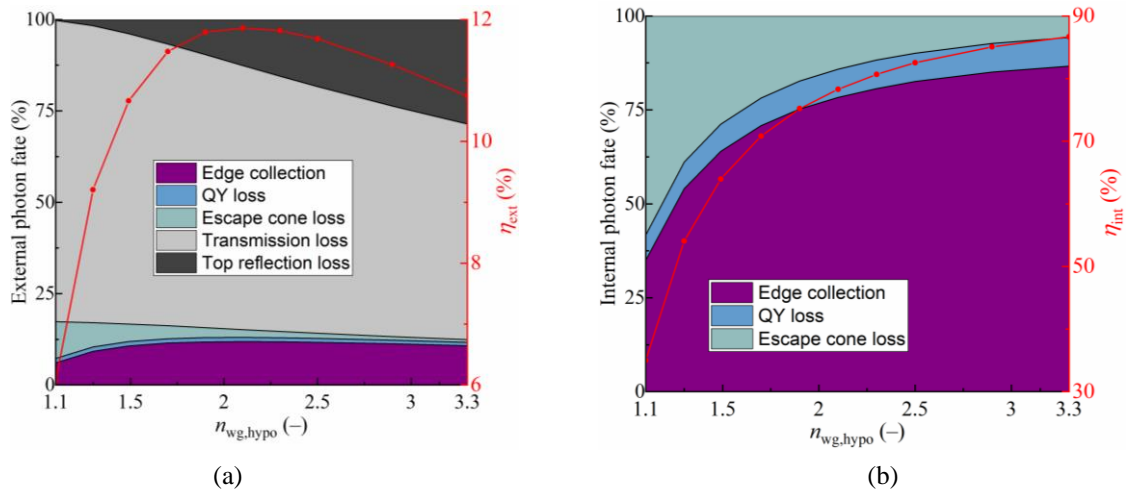


**Fig. 8.** Effect of hypothetical refractive index of the waveguide on: (a) external photon fate (left y-axis) and external photon efficiency (right y-axis), and (b) internal photon fate (left y-axis) and internal photon efficiency (right y-axis) of LSCs composed of a hypothetical waveguide material doped with LFR305 dye at a concentration of  $1 \times 10^{-4}$  mol/L. Note that all other photophysical properties and model parameters remain the same as shown in **Fig. 3** and **Table 1** (baseline values), respectively.

**Effects of PLQY and Stokes shift.** The effect of PLQY of a hypothetical luminophore on LSC performances under varying Stokes shift scenarios is shown in **Fig. 9**. Since the top reflection loss (3.9%) and the transmission loss (79.5%) remain unchanged as PLQY varies, these two terms are not illustrated in the external photon fate (right y-axis of **Fig. 9b**). A stack version of all photon fates is put in **Fig. S4**. As the PLQY increases, the QY loss drops significantly, leading to remarkable improvement in both the internal and external photon efficiencies, despite the slight increase in escape cone loss. Both efficiencies are increased by 1.5 times—from 27.6% to 67.8% for  $\eta_{\text{int}}$  and from 4.6% to 11.3% for  $\eta_{\text{ext}}$ —as PLQY grows from 0.5 to 0.99 at a Stokes shift of 33 nm. As to the effect of Stokes shift, a higher  $\Delta\lambda_{\text{S,hypo}}$  signifies less overlap between the absorption and emission spectrum thus weaker PL re-absorption, resulting in both lower QY and escape cone losses. Consequently, both efficiencies tend to increase until reaching the threshold Stokes shift at around 100 nm, above which the efficiencies begin to plateau due to the absence of re-absorption effect from zero spectral overlap. In addition, the efficiency improvement is more pronounced at lower PLQY. For instance, the increasement in both efficiencies is 74% (from 21.4% to 37.1% for  $\eta_{\text{int}}$  and from 3.6% to 6.2% for  $\eta_{\text{ext}}$ ) at a PLQY of 0.5 when  $\Delta\lambda_{\text{S,hypo}}$  rises from 0 nm to 100 nm, while that becomes only 12% (from 65.5% to 73.6% for  $\eta_{\text{int}}$  and from 10.9% to 12.3% for  $\eta_{\text{ext}}$ ) at a PLQY of 0.99.

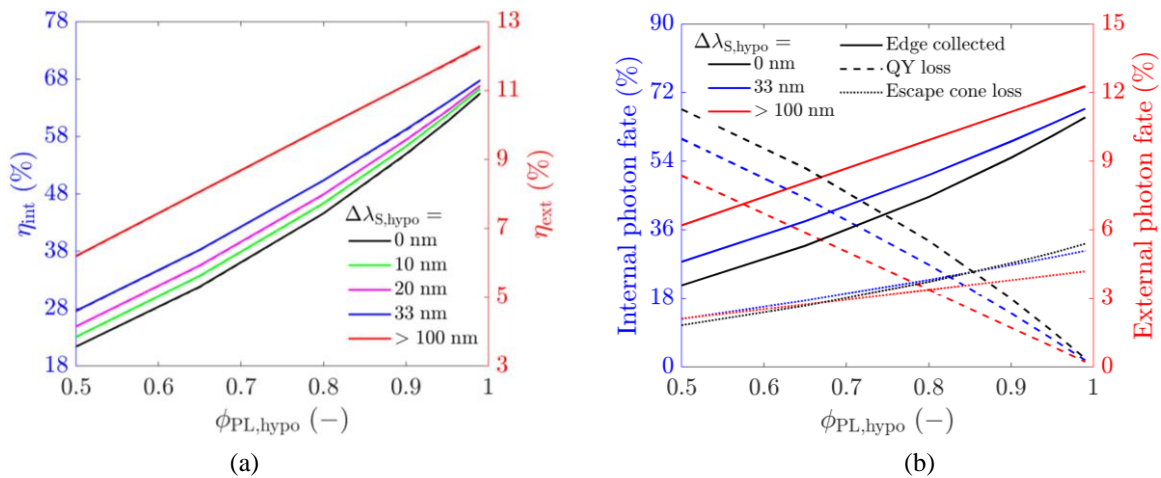


**Fig. 9.** Effect of hypothetical PLQY on: (a) internal (left y-axis) and external (right y-axis) photon efficiencies, and (b) internal (left y-axis) and external (right y-axis) photon fates of LSCs composed of PMMA as the waveguide material doped with hypothetical luminophores at varying Stokes shift scenarios. Note that all other photophysical properties and model parameters remain the same as shown in **Fig. 3** and **Table 1** (baseline values), respectively.

## 4. Conclusions

A self-consistent modelling framework of radiative transfer has been described for a generic LSC to account for the light–matter interactions at multiple length scales. A modified RTE along with its boundary conditions was rigorously derived based on radiative energy balance, and can be solved using the MC ray tracing approach. Such a framework was then applied to a specific type of square shaped LSC composed of PMMA as the waveguide doped with LFR305 dye as the luminophore, and its performance and losses has been quantified for various scenarios.

The realistic scenarios examined both the baseline performance as well as the effects of LSC dimensions and LFR305 concentration. For the baseline scenario, an external photon efficiency of 10.6% was predicted for the LSC with dimensions of  $10 \times 10 \times 0.5 \text{ cm}^3$  at a LFR305 concentration of 0.0001 mol/L. The transmission loss accounts for 79.4% of the incident photons, and is the dominating loss mechanism fundamentally due to the relatively narrow absorption spectrum of LFR305 within the solar spectrum and the non-scattering nature of LFR305. The LSC length has a minor effect on the external photon efficiency, and an efficiency drop of 6% (from 11.0% to 10.3%) is observed as LSC length increases from 5 cm to 25 cm, demonstrating good scale-up potential. By contrast, the LSC thickness and LFR305 concentration have a more pronounced effect on the LSC performance, mainly by influencing the light absorption behavior thus the transmission loss. However, the transmission loss still dominates and accounts for 76.2–92.1% depending on the specific thickness and dye concentration.

The hypothetical scenarios aimed to investigate alternative material properties for potential efficiency improvement in order to guide follow-up LSC design. As to the impact of waveguide refractive index ( $n_{\text{wg}}$ ), a non-trivial trend is observed for the external photon efficiency, revealing inevitable tradeoff of competing effects between high escape cone loss at low  $n_{\text{wg}}$  and high top reflection loss at high  $n_{\text{wg}}$ . Consequently, an optimal  $n_{\text{wg}}$  at around 2.1 exists leading to a peak  $\eta_{\text{ext}}$  of 11.9%, an increase of 12.3% as compared to the baseline performance. The hypothetical PLQY and Stokes shift are found to mainly affect the QY loss, and high PLQY combined with high Stokes shift synergistically contributes to improvement in both internal and external photon efficiencies. The best  $\eta_{\text{ext}}$  is 12.3% when PLQY is 0.99 and the Stokes shift is above 100 nm to disable the re-absorption effect. In light of these results, future improvement on LSC efficiency should be focused on mitigating the predominant transmission loss by capturing more sunlight over broadband spectrum, such as using bottom reflectors, multiple luminophores, or tandem LSC configurations.

## Nomenclature

|                                      |  |
|--------------------------------------|--|
| $A_{\text{top}}, A_{\text{edge},i}$  | area of the top surface and the edge surface $i$ of an LSC ( $\text{cm}^2$ )       |
| $c$                                  | speed of light ( $\text{m s}^{-1}$ )   |
| $c_p$                                | molar concentration of luminophore particles (mol/L)                               |
| $C_{\text{abs},p}, C_{\text{sca},p}$ | absorption and scattering cross section of a luminophore particle ( $\text{m}^2$ ) |
| $G_\lambda$                          | spectral incident radiation function ( $\text{W m}^{-2} \text{nm}^{-1}$ )          |
| $h$                                  | Planck constant ( $6.626 \times 10^{-34} \text{ J} \cdot \text{s}$ )               |
| $H_{\text{LSC}}$                     | thickness of an LSC sample (mm)  |
| $I_\lambda$                          | spectral light intensity ( $\text{W m}^{-2} \text{nm}^{-1} \text{sr}^{-1}$ )       |

|  |   |
|--|---|
| $k_{\lambda,\text{wg}}$                                    | absorptive index of the waveguide (–)                               |
| $L_{\text{LSC}}$   | length of an LSC (cm)   |
| $n_{\text{wg}}, n_{\text{wg,hypo}}$                        | refractive index of a waveguide and of a hypothetical waveguide (–) |
| $N_{\text{p}}$   | number density of luminophore particles ( $\text{m}^{-3}$ )         |
| $\dot{N}_{\lambda}$  | spectral photon rate ( $\text{s}^{-1}$ )                            |
| $P_{\text{PL}\lambda,\text{p}}$                            | photoluminescence wavelength function (–)                           |
| $\mathbf{q}_{\lambda,\text{rad}}, \mathbf{q}_{\text{rad}}$ | spectral and total radiative heat flux ( $\text{W m}^{-2}$ )        |
| $R_{\lambda,\text{wg}}$                                    | spectral reflectivity of a waveguide sample (–)                     |
| $T_{\lambda,\text{wg}}$                                    | spectral transmissivity of a waveguide sample (–)                   |
| $W_{\text{LSC}}$   | width of an LSC (cm)  |

### ***Greek symbols***

|   |   |
|---|---|
| $\alpha_{\lambda,\text{edge}}$                                      | spectral absorptivity of the edge surfaces (–)  |
| $\varepsilon_{\lambda,\text{p}}$                                    | spectral molar absorption coefficient of luminophore particles ( $\text{L mol}^{-1} \text{cm}^{-1}$ ) |
| $\delta$  | Dirac delta function (–)  |
| $\Delta\lambda_{\text{S}}$  | Stokes shift (nm)   |
| $\eta_{\text{int}}, \eta_{\text{ext}}$                              | internal and external photon efficiency (–)   |
| $\theta_{\text{in}}, \theta'_{\text{in}}$                           | dummy angles of incidence ( $^{\circ}$ )  |
| $\kappa_{\lambda}$  | spectral absorption coefficient ( $\text{cm}^{-1}$ )  |
| $\lambda, \bar{\lambda}_{\text{abs}}, \bar{\lambda}_{\text{PL}}$    | wavelength of light, mean absorption and photoluminescence spectrum (nm)                              |
| $\nu$   | frequency of light ( $\text{s}^{-1}$ )  |
| $\rho_{\lambda}$  | spectral bi-directional reflectivity (–)  |
| $\sigma_{\text{s},\lambda}$   | spectral scattering coefficient ( $\text{cm}^{-1}$ )  |
| $\phi_{\text{PL}}$  | photoluminescence quantum yield (–)   |
| $\varphi$   | azimuthal angle ( $^{\circ}$ )  |
| $\Phi_{\text{PL}\lambda,\text{p}}, \Phi_{\text{s}\lambda,\text{p}}$ | photoluminescence and scattering phase function (–)   |
| $\Omega, \Omega', \Omega''$   | solid angles (sr)   |

### ***Subscripts***

|            |                          |
|------------|--------------------------|
| 0          | vacuum condition         |
| abs        | absorption               |
| btm        | bottom surface of an LSC |
| hypo       | hypothetical             |
| in         | incidence direction      |
| p          | luminophore particles    |
| r, refract | refraction direction     |
| rad        | radiative                |
| S          | Stokes shift             |
| s, sca     | scattering               |
| w          | wall                     |
| wg         | waveguide                |

### ***Abbreviations***

|        |                                |
|--------|--------------------------------|
| LFR305 | Lumogen F Red 305              |
| LSC    | luminescent solar concentrator |
| MC     | Monte Carlo                    |

|      |                             |
|------|-----------------------------|
| PL   | photoluminescence           |
| PMMA | poly(methyl methacrylate)   |
| QY   | quantum yield               |
| RHS  | right-hand side             |
| RTE  | radiative transfer equation |
| TIR  | total internal reflection   |

### **CRedit authorship contribution statement**

**Sha Li:** Conceptualization, Methodology, Investigation, Writing – original draft. **Sophia Haussener:** Conceptualization, Methodology, Writing—review & editing, Supervision, Project administration, Funding acquisition.

### **Declaration of competing interest**

The authors declare that they have no known competing financial interests or personal relationships that could have appeared to influence the work reported in this paper.

### **Data availability**

Data will be made available on request.

### **Acknowledgements**

The financial support from the EU's Horizon 2020 SPOTLIGHT Project (Grant Agreement No.101015960) funded by the Photonics Public Private Partnership Programme is gratefully acknowledged.

### **Appendix A: Supplementary material**

Supplementary data to this article can be found online at <http://xxx>.

### **References**

- [1] Papakonstantinou I, Portnoi M, Debije MG. The Hidden Potential of Luminescent Solar Concentrators. *Advanced Energy Materials*. 2020;11(3):2002883.
- [2] Gungor K, Du J, Klimov VI. General Trends in the Performance of Quantum Dot Luminescent Solar Concentrators (LSCs) Revealed Using the “Effective LSC Quality Factor”. *ACS Energy Letters*. 2022;7(5):1741–9.
- [3] Chatten A, Barnham K, Buxton B, Ekins-Daukes N, Malik M. Quantum dot solar concentrators. *Semiconductors*. 2004;38:909–17.
- [4] Chatten A, Farrel D, Jermyn C, Thomas P, Buxton B, Buchtemann A, et al. Thermodynamic modelling of luminescent solar concentrators. *Conference Record of the Thirty-first IEEE Photovoltaic Specialists Conference, 2005*: IEEE; 2005. p. 82–5.
- [5] Yablonovitch E. Thermodynamics of the fluorescent planar concentrator. *JOSA*. 1980;70(11):1362–3.
- [6] Farrell DJ, Chatten AJ, Buchtemann A, Barnham KW. Fabrication, characterisation & modelling of quantum dot solar concentrator stacks. *2006 IEEE 4th World Conference on Photovoltaic Energy Conference*: IEEE; 2006. p. 217–20.
- [7] Carrascosa M, Unamuno S, Agulló-López F. Monte Carlo simulation of the performance of PMMA luminescent solar collectors. *Appl Opt*. 1983;22(20):3236–41.
- [8] Zhang B, Yang H, Warner T, Mulvaney P, Rosengarten G, Wong WWH, et al. A luminescent solar concentrator ray tracing simulator with a graphical user interface: features and applications. *Methods Appl Fluoresc*. 2020;8(3):037001.

- [9] Smith DE, Hughes MD, Patel B, Borca-Tasciuc D-A. An Open-Source Monte Carlo Ray-Tracing Simulation Tool for Luminescent Solar Concentrators with Validation Studies Employing Scattering Phosphor Films. *Energies*. 2021;14(2):455.
- [10] Kennedy M, Chatten A, Farrell D, Bose R, Büchtemann A, McCormack S, et al. Thermodynamic modelling and ray-trace modelling of luminescent solar concentrators: A comparison of the two approaches. *23rd European Photovoltaic Solar Energy Conference and Exhibition* 2008. p. 334–7.
- [11] Modest MF. *Radiative Heat Transfer*. Third Edition ed: Academic Press; 2013. 279–300 p.
- [12] Haussener S, Lipiński W, Petrasch J, Wyss P, Steinfeld A. Tomographic Characterization of a Semitransparent-Particle Packed Bed and Determination of its Thermal Radiative Properties. *Journal of Heat Transfer*. 2009;131(7).
- [13] Dai X, Haussener S. Optical characterization of multi-scale morphologically complex heterogeneous media—Application to snow with soot impurities. *Journal of Quantitative Spectroscopy and Radiative Transfer*. 2018;206:378–91.
- [14] Hughes MD, Borca-Tasciuc DA, Kaminski DA. Method for modeling radiative transport in luminescent particulate media. *Appl Opt*. 2016;55(12):3251–60.
- [15] Alinejad F, Bordbar H, Makowska M, Hostikka S. Spectroscopic determination of the optical constants and radiative properties of black PMMA for pyrolysis modeling. *International Journal of Thermal Sciences*. 2022;176:107501.
- [16] Kaniyoor A, McKenna B, Comby S, Evans RC. Design and Response of High-Efficiency, Planar, Doped Luminescent Solar Concentrators Using Organic-Inorganic Di-Ureasil Waveguides. *Advanced Optical Materials*. 2016;4(3):444–56.
- [17] Dramićanin M. *Luminescence thermometry: methods, materials, and applications*: Woodhead Publishing; 2018. 33–61 p.
- [18] Du K, Li H, Guo K, Wang H, Li D, Zhang W, et al. The rate equation based optical model for phosphor-converted white light-emitting diodes. *Journal of Physics D: Applied Physics*. 2017;50(9):095101.
- [19] Ma Y, Sun J, Luo X. Multi-wavelength phosphor model based on fluorescent radiative transfer equation considering re-absorption effect. *Journal of Luminescence*. 2019;209:109–15.
- [20] Yalcin RA, Erturk H. Monte Carlo method solution of the broadband fluorescent radiative transfer equation considering fluorescent cascade. *Appl Opt*. 2021;60(4):1068–77.
- [21] Bohren CF, Huffman DR. *Absorption and scattering of light by small particles*: John Wiley & Sons; 2008. 12–56 p.
- [22] Draine BT, Flatau PJ. Discrete-dipole approximation for scattering calculations. *Josa a*. 1994;11(4):1491–9.
- [23] Chen J, Wheeler VM, Liu B, Kumar A, Coventry J, Lipiński W. Optical characterisation of alumina–mullite materials for solar particle receiver applications. *Solar Energy Materials and Solar Cells*. 2021;230:111170.
- [24] Oster G. The scattering of light and its applications to chemistry. *Chemical reviews*. 1948;43(2):319–65.
- [25] Oster G, Riley DP. Scattering from isotropic colloidal and macro-molecular systems. *Acta Crystallographica*. 1952;5(1):1–6.
- [26] Tummeltshammer C, Taylor A, Kenyon AJ, Papakonstantinou I. Losses in luminescent solar concentrators unveiled. *Solar Energy Materials and Solar Cells*. 2016;144:40–7.
- [27] Zhang B, Soleimaninejad H, Jones DJ, White JM, Ghigginio KP, Smith TA, et al. Highly Fluorescent Molecularly Insulated Perylene Diimides: Effect of Concentration on Photophysical Properties. *Chemistry of Materials*. 2017;29(19):8395–403.
- [28] Hughes MD, Maher C, Borca-Tasciuc D-A, Polanco D, Kaminski D. Performance comparison of wedge-shaped and planar luminescent solar concentrators. *Renewable Energy*. 2013;52:266–72.
- [29] Debije MG, Evans RC, Griffini G. Laboratory protocols for measuring and reporting the performance of luminescent solar concentrators. *Energy & Environmental Science*. 2021;14(1):293–301.

- [30] Cambié D, Zhao F, Hessel V, Debije MG, Noel T. A Leaf-Inspired Luminescent Solar Concentrator for Energy-Efficient Continuous-Flow Photochemistry. *Angew Chem Int Ed Engl*. 2017;56(4):1050–4.
- [31] Griffini G, Levi M, Turri S. Thin-film luminescent solar concentrators: A device study towards rational design. *Renewable Energy*. 2015;78:288–94.
- [32] Tatsi E, Fortunato G, Rigatelli B, Lyu G, Turri S, Evans RC, et al. Thermoresponsive Host Polymer Matrix for Self-Healing Luminescent Solar Concentrators. *ACS Applied Energy Materials*. 2019;3(1):1152–60.
- [33] Ostos FJ, Iasilli G, Carlotti M, Pucci A. High-Performance Luminescent Solar Concentrators Based on Poly(Cyclohexylmethacrylate) (PCHMA) Films. *Polymers (Basel)*. 2020;12(12).
- [34] Zettl M, Mayer O, Klampaftis E, Richards BS. Investigation of host polymers for luminescent solar concentrators. *Energy Technology*. 2017;5(7):1037–44.
- [35] Ma Y, Wang M, Sun J, Hu R, Luo X. Phosphor modeling based on fluorescent radiative transfer equation. *Opt Express*. 2018;26(13):16442–55.
- [36] Klimov VI, Baker TA, Lim J, Velizhanin KA, McDaniel H. Quality Factor of Luminescent Solar Concentrators and Practical Concentration Limits Attainable with Semiconductor Quantum Dots. *ACS Photonics*. 2016;3(6):1138–48.
- [37] Wilson LR. *Luminescent solar concentrators: a study of optical properties, re-absorption and device optimisation*, PhD thesis, Heriot-Watt University Edinburgh; 2010.
- [38] Hughes MD, Borca-Tasciuc D-A, Kaminski DA. Highly efficient luminescent solar concentrators employing commercially available luminescent phosphors. *Solar Energy Materials and Solar Cells*. 2017;171:293–301.
- [39] Cambié D, Zhao F, Hessel V, Debije MG, Noël T. Every photon counts: understanding and optimizing photon paths in luminescent solar concentrator-based photomicroreactors (LSC-PMs). *Reaction Chemistry & Engineering*. 2017;2(4):561–6.
- [40] Farrell D, Farrell D. Pvtrace: Optical Ray Tracing for Luminescent Materials and Spectral Converter Photovoltaic Devices. 2019.

# Supplementary Material

## Radiative Transfer in Luminescent Solar Concentrators

Sha Li, Sophia Haussener\*

Laboratory of Renewable Energy Science and Engineering, EPFL, Station 9, Lausanne 1015, Switzerland

### 1. AM 1.5 standard direct solar spectral irradiance

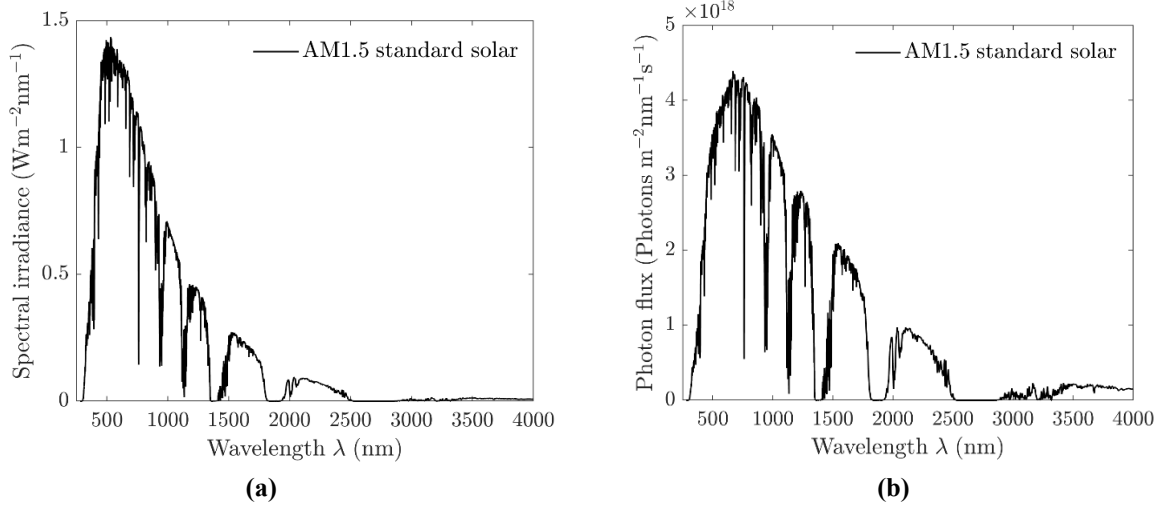


Fig. S1. AM 1.5 standard solar spectral (a) irradiance and (b) photon flux from Ref. [1].

### 2. Monte Carlo ray tracing flowchart

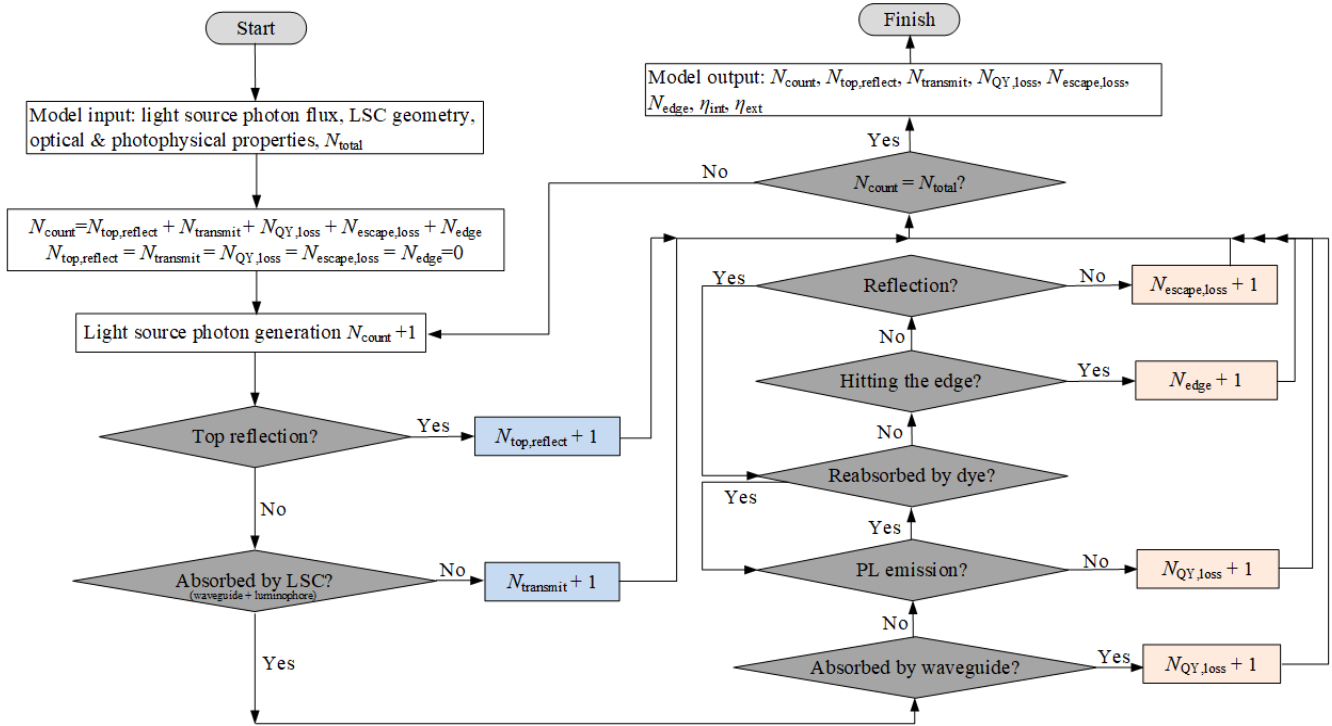


Fig. S2. Monte Carlo ray tracing flowchart

\* Corresponding author.

E-mail address: [sophia.haussener@epfl.ch](mailto:sophia.haussener@epfl.ch) (S. Haussener).

### 3. Ray number independence check

**Table S1.** Ray number independence check for the baseline case

| Ray number        | $\eta_{\text{ext}}$ | $\eta_{\text{int}}$ | Edge collected | QY loss | Escape cone loss | Transmission loss | Top reflection loss |
|-------------------|---------------------|---------------------|----------------|---------|------------------|-------------------|---------------------|
| $6.0 \times 10^4$ | 10.75%              | 64.23%              | 10.75%         | 1.23%   | 4.75%            | 79.46%            | 3.81%               |
| $6.0 \times 10^5$ | 10.68%              | 64.10%              | 10.68%         | 1.20%   | 4.79%            | 79.44%            | 3.89%               |
| $9.0 \times 10^6$ | 10.66%              | 63.97%              | 10.66%         | 1.21%   | 4.80%            | 79.45%            | 3.88%               |
| $3.6 \times 10^7$ | 10.66%              | 63.97%              | 10.66%         | 1.21%   | 4.80%            | 79.45%            | 3.88%               |

### 4. Model validation

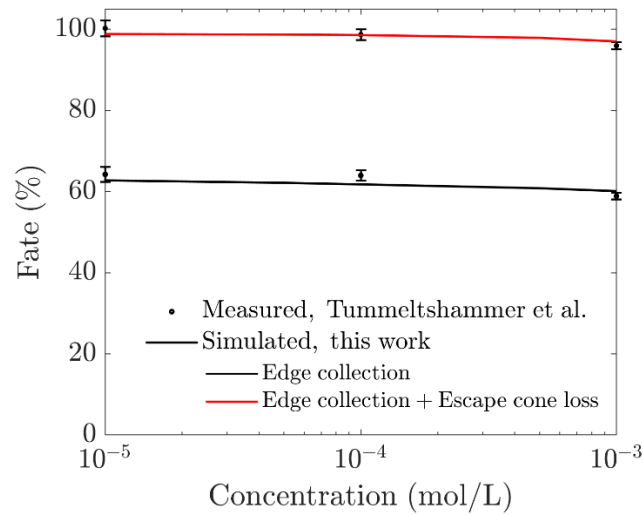


**Fig. S3.** Comparison between measurement by Tummeltshammer et al. [2] and Monte Carlo ray tracing simulation from this work for LSCs doped with Coumarin 6 at varying dye concentrations.

## 5. Performance analysis

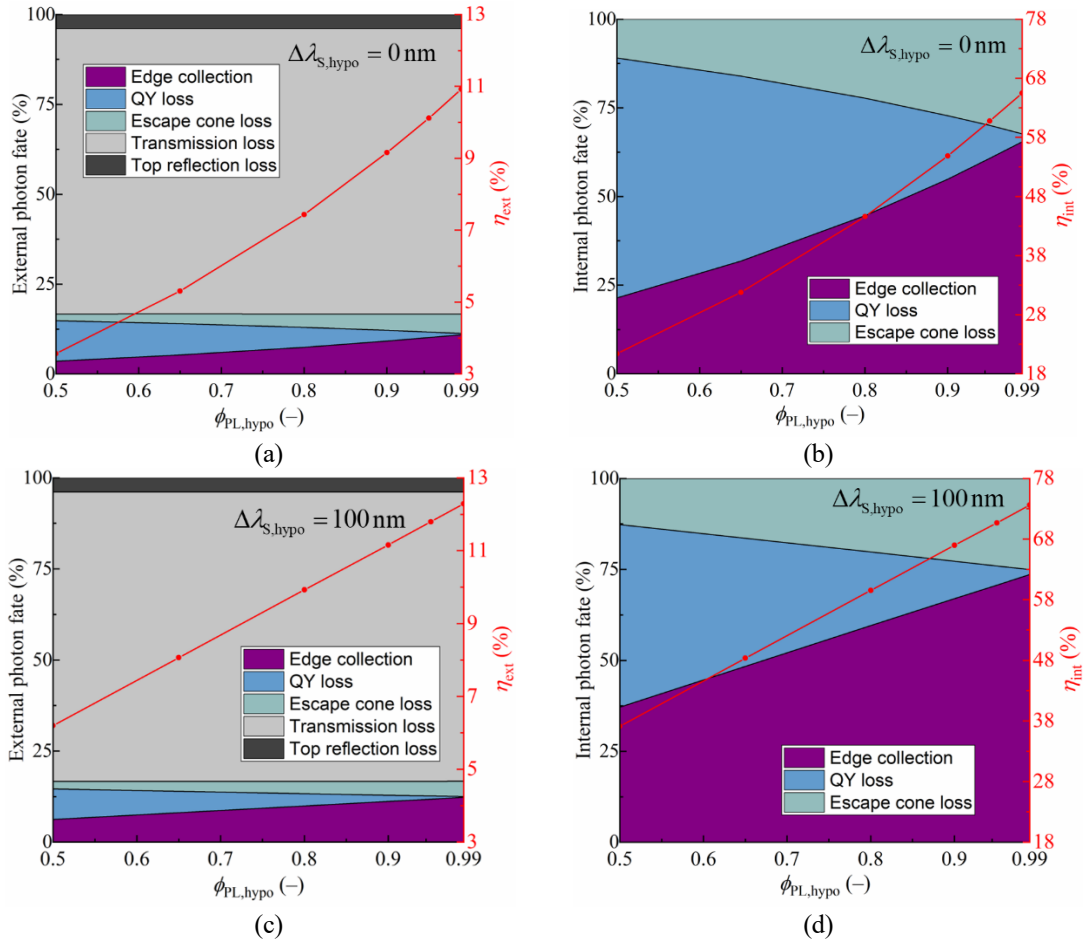


**Fig. S4.** Effect of hypothetical PLQY on: (a) (c) external photon fate (left y-axis) and external photon efficiency (right y-axis), and (b) (d) internal photon fate (left y-axis) and internal photon efficiency (right y-axis) of LSCs composed of PMMA doped with hypothetical luminophores at varying scenarios of Stokes shift for (a) (b) 0 nm, and (c) (d) 100 nm. Note that all other photophysical properties and model parameters remain the same as shown in **Fig. 3** and **Table 1** (baseline values), respectively.

## References

- [1] ASTM G-173-03, Standard Tables for Reference Solar Spectral Irradiances: Direct Normal and Hemispherical on 37° Tilted Surface. 2020.
- [2] Tummeltshammer C, Taylor A, Kenyon AJ, Papakonstantinou I. Losses in luminescent solar concentrators unveiled. *Solar Energy Materials and Solar Cells*. 2016;144:40–7.